PHYSICAL REVIEW B VOLUME 51, NUMBER 15 15 APRIL 1995-I

Nonresonant carrier transport through high-field domains in semiconductor superlattices

S.H. Kwok, H.T. Grahn, M. Ramsteiner, and K. Ploog
Paul-Drude-Institut für Festkörperelektronik, Hausvogteiplatz 5-7, D-10117 Berlin, Germany

F. Prengel, A. Wacker, and E. Schöll
Institut für Theoretische Physik, Technische Universität Berlin, Hardenbergstraße 36, D-10623 Berlin, Germany

S. Murugkar and R. Merlin
The Harrison M. Randall Laboratory of Physics, The University of Michigan, Ann Arbor, Michigan 48109-1120
(Received 7 October 1994)

The actual field distribution in superlattices under electric field domain formation is investigated by photoluminescence and Raman spectroscopy. From the measured subband spacings, we determine the magnitude of the field that corresponds to resonant alignment of subbands in adjacent wells. The electron occupation of higher subbands is probed by photoluminescence (PL) measurements. Comparing the results of higher subband PL and the current-voltage characteristics, it is shown that the high-field domain is always nonresonantly coupled with a field strength below the resonance value. The sudden increase in the current when the high-field domain extends over the entire superlattice is explained. Calculations of the field distribution based on a microscopic model support our experimental observations.

I. INTRODUCTION

The dominant transport mode normal to the layers in semiconductor superlattices is resonant tunneling. In weakly coupled superlattices, negative differential resistance due to sequential resonant tunneling has been predicted theoretically.[1] Capasso *et al.*[2] observed two peaks due to resonant tunneling from the lowest conduction subband into the second as well as the third conduction subband in static photocurrent experiments. The situation changes drastically when the carrier density in the structures is large. In this case oscillatory structures appear in the photocurrent-voltage characteristic.[3] This was explained by spontaneous formation of two regions of different field strengths, i.e., electric field domains. The domain boundary consists of a space charge layer, which compensates the field gradient between the two domains. The oscillatory behavior is attributed to the migration of the domain boundary across the sample with increasing voltage. Its period corresponds approximately to the subband separation in the superlattice.

Electric field domains in superlattices were, to our knowledge, first discovered by Esaki and Chang[4] in conductance measurements. In recent years, the studies of electric field domains have received considerable attention. The oscillatory structures in the current-voltage measurement have been repeatedly observed by many groups.[3,5–13] A direct proof of domain formation has been conducted by photoluminescence (PL) spectroscopy. Due to the existence of two regions of different field strengths, PL emissions associated with the high-field and low-field domains experience different Stark shifts.[3] Consequently, two peaks can be observed in the PL measurement. The energies of the PL peaks provide a measure of the magnitude of the field in the wells through the quantum-confined Stark effect.[14] The field strengths were shown to be approximately equal to the subband spacing divided by the electric charge and superlattice period. Several theoretical models of domain formation have been proposed in the past few years.[3,15–18]

It has been customary to assume that electrons tunnel resonantly within domains. However, in a recent paper, we have demonstrated that higher subband photoluminescence (HSPL) spectroscopy can be used to determine the actual field strengths of domains.[19] Nonresonant tunneling was shown to be the dominant transport mode in the high-field domain with a field strength slightly below the resonant tunneling condition. A simple model of current conservation was used to explain our observations. The present paper reports on a detailed study of the actual electric field distribution within superlattices under domain formation. The HSPL emissions from different domains can be resolved. As a result we can investigate the behavior of different domains unambiguously. By using a physically motivated model,[17] we can calculate the field distribution within the superlattice as a function of external voltage. The theoretical calculations agree well with the experimental results.

The organization of this paper is as follows. In the next section, we describe the details of sample parameters and the experimental conditions. In Sec. III, we report on the determination of the subband spacings by Raman scattering and HSPL measurements. In Sec. IV, we compare the intensities of HSPL with the *I-V* characteristic and interpret the data. Calculations of the field distribution using a microscopic model are presented in

0163-1829/95/51(15)/9943(9)/$06.00

Sec. V. Finally, in Sec. VI we summarize our results and draw conclusions.

II. SAMPLE PREPARATION AND EXPERIMENTAL DETAILS

The samples have been grown by molecular beam epitaxy on (001) n^+-GaAs substrates. Experimental results on four samples are presented. Their parameters are listed in Table I. Samples 1, 2, and 3 are undoped, while the central 5 nm of each well in sample 4 is doped with Si donors at a density of $n = 3 \times 10^{17}$ cm^{-3}. The superlattices are sandwiched between heavily doped layers to form p^+-i-n^+ (samples 1–3) and n^+-n-n^+ (sample 4) structures. To avoid depletion regions, graded layers are inserted between the superlattice region and the heavily doped layers. The samples are processed into mesas of area between 0.01 and 0.16 mm^2 with Ohmic Cr/Au contacts on the top and AuGe/Ni contacts on the bottom. Because of the doping in sample 4, it exhibits domain formation in the dark, while photoexcitation is used to generate a large carrier density and, thus, domain formation in the undoped structures. The latter show dark currents below 1 nA in reverse bias. Typical excitation powers are between 10 and 60 mW. The diameter of the focus is $\sim$ 100 μm. All measurements were performed below 10 K.

Band-gap PL spectra were measured using an Ar$^+$-laser-pumped tunable Ti:sapphire laser with an excitation energy $\hbar\omega_L = 1.722$ eV. The HSPL spectra were obtained using the 1.916 and 1.833 eV lines of a Kr$^+$ laser. Resonant Raman measurements of sample 1 and 2 were performed using the 1.916 eV Kr$^+$ line and an Ar$^+$-laser-pumped tunable dye laser with $\hbar\omega_L = 1.943$ eV, respectively. These energies were chosen in order to match the resonant condition at the superlattice critical point derived from the $E_0 + \Delta_0$ gap of GaAs. Spectra were recorded in the $z(x', x')\bar{z}$ and $z(y', x')\bar{z}$ configurations where x', y', and z denote the [110], [1$\bar{1}$0], and [001] directions, respectively. Since the intensity of HSPL is many orders of magnitude weaker than the band-gap PL, a Raman setup (Dilor X-Y multichannel system) was used to measure these signals. The band-gap PL was measured using a 1-m single monochromator with a liquid nitrogen cooled charge coupled device detection system. Current-voltage characteristics were recorded using a Keithley 236 source measure unit.

III. MEASUREMENT OF THE SUBBAND SPACINGS

The knowledge of the electron subband spacings in superlattices is very important for electric field domain studies because it determines the field at which resonant tunneling occurs, i.e., $F_i = (E_i - E_1)/(ed)$, where E_i is the energy of the ith subband. We will label the electron subbands by e_i and the heavy-hole ground state by h_1. The approximate field strengths of domains can be estimated since domain j is associated with the $e_1 \rightarrow e_j$ tunneling resonance. Two optical techniques are used to measure the subband spacings of superlattices. Raman scattering by intersubband excitation is an effective way to measure the separation between subbands. The spin-density peak energy is close to the actual separation of the subbands. The relatively narrow line shape of Raman peaks allows a precise determination of the subband spacings.[20] Higher subband ($e_j h_1$) PL refers to the emission due to recombination of electrons in the jth subband and heavy holes in the first subband. Neglecting the difference in binding energies for $e_j h_1$ and $e_1 h_1$ excitons, the energetic separation between $e_j h_1$ and $e_1 h_1$ PL is also a good estimate of the subband spacing between e_1 and e_j. Compared to absorption experiments, the identification of $e_j h_1$ exciton peaks is more reliable because only transitions involving the first hole subband are dominant. The $e_j h_1$ transitions are nominally forbidden in infinitely deep wells and at zero field, but their oscillator strength becomes nonzero under the application of an electric field. Figure 1 illustrates schematically the $e_j h_1$ interband and the $e_1 e_j$ intersubband transitions.

The Raman spectra of sample 1 at -2 V are shown in Fig. 2. Besides the two longitudinal-optical (LO) phonon peak at 73 meV a broader peak appears at 61.5 meV in the depolarized and at 67 meV in the polarized Raman spectrum. These peaks are ascribed to the $e_1 e_2$ intersubband transition of photoexcited electrons due to spin-density and charge-density excitations in the depolarized $[z(y', x')\bar{z})]$ and polarized $[z(x', x')\bar{z}]$ spectrum, respectively. The assignment of these peaks is consistent with the observed laser power and voltage dependence. In particular, the intensity of the intersubband peak increases nonlinearly with the laser power. A significant shift (5 meV) is observed between the charge-density and the spin-density peak position.[20] Due to the blueshift of the subband spacing with increasing field, the energy of the peak increases at higher voltages.[21] Therefore, we determine the subband spacing using only the spectra at voltages, that are in the vicinity of corresponding tunneling resonances. In sample 1, the $e_1 \rightarrow e_2$ resonance occurs at -2 V. Based on the position of the spin-density peak, we estimate that the $e_2 - e_1$ separation of sample 1 at -2 V is 61.5 meV. Similar measurements have been carried out for other samples[19,22] and the corresponding subband spacings are listed in Table II.

The occupation of higher subbands by resonant tun-

TABLE I. Sample parameters.

Sample	Well width/material	Barrier width/material	No. of periods	Built-in voltage
1	14.4 nm/ GaAs	3.4 nm/ AlAs	50	1.3 V
2	13.1 nm/ GaAs	7.9 nm/ $Al_{0.35}Ga_{0.65}As$	100	1.5 V
3	9.0 nm/ GaAs	4.0 nm/ AlAs	40	1.5 V
4	9.0 nm/ GaAs	4.0 nm/ AlAs	40	0 V

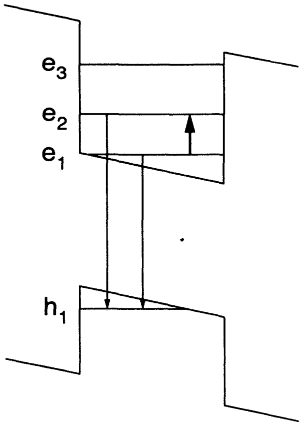

FIG. 1. Schematic diagram showing the interband emission transitions e_1h_1 and e_2h_1 as well as the intersubband transition e_1e_2 in a quantum well in an applied electric field.

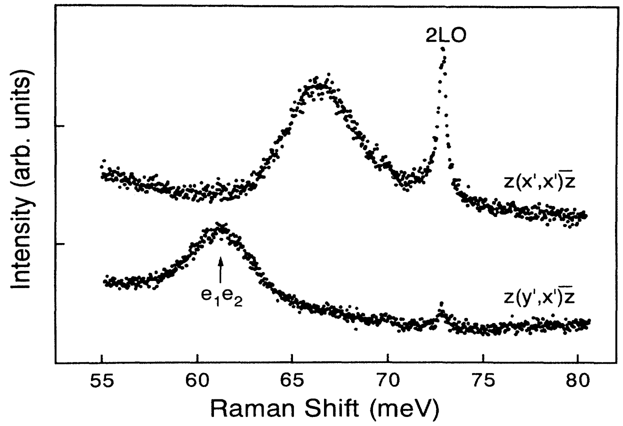

FIG. 2. Polarized $[z(x',x')\bar{z}]$ and depolarized $[z(y',x')\bar{z}]$ Raman spectra of sample 1 at an applied voltage of -2 V. The narrow feature at 73 meV is due to scattering by two LO phonons. The intersubband spin-density excitation is labeled e_1e_2. The peak at 67 meV in the polarized spectrum is its charge-density companion.

neling can be studied directly by photoluminescence and electroluminescence measurements.[23–26] At low temperatures, electrons are injected by resonant tunneling from the first subband into a higher subband in the adjacent well followed by a relaxation into the ground state via intersubband scattering. Figure 3 reproduces the e_1h_1, e_2h_1, and e_3h_1 PL spectra at different voltages for sample 1. Two e_1h_1 PL peaks are observed between -2 V and -5.4 V while three peaks are seen at voltages below -8 V. Previously, two e_1h_1 peaks were also detected between 1.5 V and -1.4 V at a different excitation power.[3] The e_2h_1 PL peak clearly emerges at about -2 V and the e_3h_1 PL peak appears at voltages below -5 V. Due to the large well width of this sample, the Stark shifts of the PL peaks at larger fields are significant. As a result we can clearly resolve the HSPL associated with different domains for the first time. Two e_2h_1 PL peaks are seen at voltages between -4.8 and -5.4 V, while two e_3h_1 are observed between -9.7 and -12.7 V.

A comparison of the peak energies of the e_1h_1, e_2h_1, and e_3h_1 PL lines is illustrated in Fig. 4. To facilitate our discussion, we divide the diagram into several voltage regions by using vertical solid lines. I-II, II-III, and III-IV-V label the regions of coexistence of two or three domains. These are the regions where electric field domains exist according to the PL measurements. It will be shown later that these assignments are also consistent with the photocurrent measurements. For example, I-II stands for the region of coexistence of domain I and II. The regions denoted by first TR and second TR are the transition regions between different domain regimes. We will discuss the origin of these intermediate regions in the next section. In the e_1h_1 spectra, two peaks are detected in the II-III region. However, three peaks are observed in the III-IV-V region. The additional line between the PL peaks associated with domain III and IV was previously assigned as a region (domain V) due to resonant alignment between e_2 and e_4.[3] However, since the e_2 subband is not significantly occupied, this assignment cannot be sustained. The origin of this peak is at the moment unclear. The e_1h_1 PL spectra clearly show that several regions of well-defined field strengths can coexist in the sample. In the e_2h_1 and e_3h_1 spectra only two peaks are observed in the II-III and III-IV-V region, respectively.

TABLE II. Conduction subband spacings determined by Raman scattering and higher subband photoluminescence (HSPL) measurements.

Sample	Subband spacings	Raman scattering (meV)	Higher subband PL (meV)	Calculated (meV)
1	$E_2 - E_1$	61.5	61	60
	$E_3 - E_1$		163	162
2	$E_2 - E_1$	59.5	60	64
	$E_3 - E_1$		146	167
3	$E_2 - E_1$	142	141	137
4	$E_2 - E_1$	137	138	137

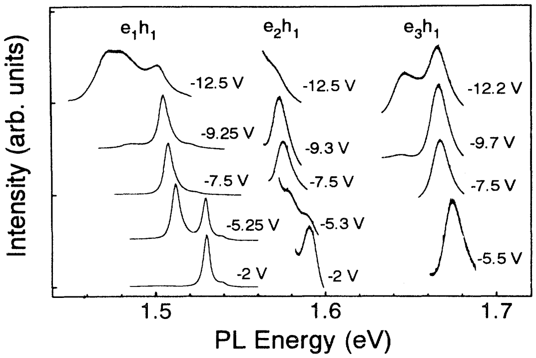

FIG. 3. e_1h_1 (left), e_2h_1 (middle), and e_3h_1 (right) photoluminescence spectra of sample 1 at different voltages.

We did not try to resolve the two e_1h_1 PL lines in the I-II regime, since there is no signal from higher subbands.

The differences in energies between the e_1h_1 and e_jh_1 ($j = 2, 3$) PL lines are listed in Table II. Similar measurements have been performed on sample 2, 3, and 4. The subband spacings determined by Raman scattering and HSPL measurements are the same within experimental errors. The $e_1 \rightarrow e_j$ resonant tunneling voltage (U_{1j}) can be calculated using

$$U_{1j} = -\frac{(E_j - E_1)W}{e\,d} + U_{\rm BI}, \qquad (1)$$

where W is the width of the intrinsic region, d the superlattice period, and $U_{\rm BI}$ the built-in voltage of diode.

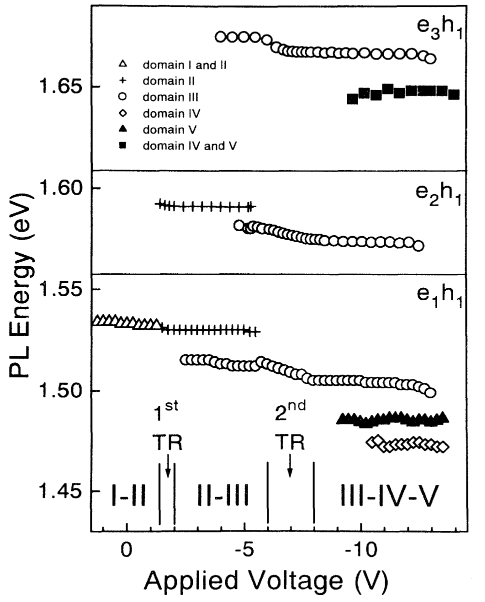

FIG. 4. PL energies for sample 1. The vertical solid lines separate single domain transition regions (TR) from those of domain coexistence (I-II, II-III, and III-IV-V).

$W = Nd + 2l_{\rm GaAs}$, where N denotes the number of periods and $l_{\rm GaAs}$ the width of the undoped GaAs layers between the superlattice and the graded layers. Using the measured subband spacings, we calculate U_{1j} for different samples.

The theoretical values of subband spacings are also calculated by solving numerically the Schrödinger equation for a single quantum well. The calculated subband spacings are comparable to the measured values (see Table II). For sample 2, the difference between the calculated and measured values can be accounted for by using a slightly larger well width in the calculations.

IV. COMPARISON OF THE VOLTAGE DEPENDENCE OF THE HIGHER SUBBAND PHOTOLUMINESCENCE INTENSITIES AND THE CURRENT

Under steady-state and spatially uniform conditions, the ratio between the electron concentration in the jth subband (n_j) and the first subband (n_1) at resonant field F_j is given by

$$\frac{n_1}{n_j} = \tau_{\rm tran}\sum_{k=1}^{j-1}\frac{1}{\tau_{jk}} = \frac{\tau_{\rm tran}}{\tau_j}, \qquad (2)$$

where τ_{jk} is the intersubband scattering time from jth to the kth subband, τ_j is the effective intersubband scattering time, and $\tau_{\rm tran}$ is the well-to-well transit time at resonance from e_1 to e_j. In Eq. (2), we assume that the tunneling time out of the higher subbands and the electron-hole recombination time are large compared to the intersubband scattering time. This is justified since τ_j is typically smaller than 1 ps for subband spacing larger than the LO phonon energy (36 meV).[23] Moreover, the carriers are assumed to be present mainly in the first subband. For weakly coupled superlattices, $\tau_{\rm tran}$ is of the order of nanoseconds. Therefore, n_j is expected to be at least three orders of magnitude smaller than n_1. Experimentally, the ratio of e_1h_1 to e_jh_1 PL intensity is 10^4–10^6. This ratio is a good estimate of n_1/n_j provided that the correction factors due to different oscillator strengths of e_1h_1 and e_jh_1 transitions are included. The relationship between e_jh_1 PL intensity and the current due to $e_1 \rightarrow e_j$ resonant tunneling can be approximately obtained as follows. The current density J is equal to the two-dimensional electron density divided by $\tau_{\rm tran}$. Together with Eq. (2), we have

$$J \simeq \frac{n_1}{\tau_{\rm tran}} = \frac{n_j}{\tau_j} \quad . \qquad (3)$$

The variation of τ_j with field is small.[27] Under the condition of $e_1 \rightarrow e_j$ resonant tunneling, the current and the electron concentration in the jth subband increase drastically due to reduction of $\tau_{\rm tran}$. Therefore, the observation of an increase of the e_jh_1 PL intensity is a definite signature that the bias of the sample is approaching the resonant tunneling condition. This allows one to determine whether the field strength of a domain is equal to or below the corresponding resonant field value.

At very low excitation power ($\sim 10^{-6}$ W), there is no structure in the I-V measurement of sample 1. As shown in Fig. 5(a), the photocurrent-voltage characteristic exhibits clear oscillatory structures when the excitation power is increased to 40 mW. The same notations as in Fig. 4 are used to label different domain regions. The three current plateau regions are denoted by I-II, II-III, and III-IV-V. Consistent with the PL measurements, oscillatory structures are seen in regions, where two or three domains coexist. The number of discontinuities in each plateau is of the order of the number of superlattice periods. Between the different current plateaus, there are transition regions where the current rises abruptly. The single e_1h_1 PL peak suggests that only one domain remains in these transition regions. In Figs. 5(b) and (c), we compare the voltage dependence of the e_2h_1 and the e_3h_1 PL intensities with the photocurrent for sample 1. In the I-II region, no e_2h_1 PL signal is detectable. This clearly demonstrates that domain II exhibits a field strength below the resonant field F_2 in this region. The e_2h_1 PL line emerges only at about -1.4 V with its intensity increasing together with the photocurrent in the first transition region. Both the photocurrent and the e_2h_1 PL intensity peak at about -2 V, which is consistent with the value of resonant condition predicted from the measured subband spacing. These results also imply that only one domain remains in the first transition region, and its field strength increases to a value that corresponds to the field strength of the $e_1 \rightarrow e_2$ tunneling resonance.

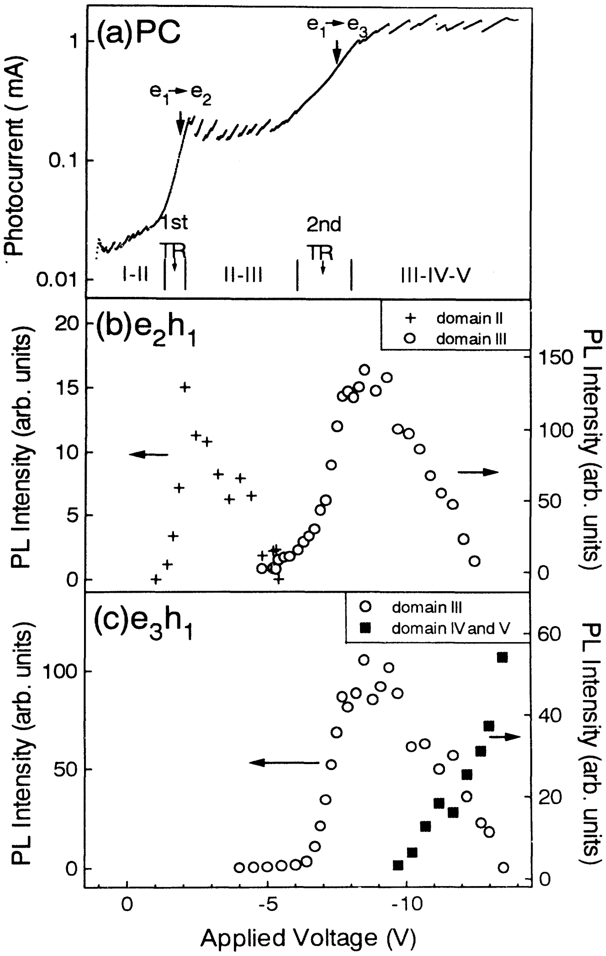

FIG. 5. (a) Photocurrent vs applied voltage for sample 1. The arrows denote the voltage corresponding to the $e_1 \rightarrow e_2$ and $e_1 \rightarrow e_3$ alignment as determined from the optical data. (b) and (c) PL intensity of the higher subband transitions vs applied voltage.

In the II-III region, two e_2h_1 peaks are observed. The intensity of the e_2h_1 PL peak associated with domain II decreases with increasing voltage because of the length reduction of domain II. The *linear* decrease of its intensity suggests that the low-field domain (II) remains almost resonantly coupled as it contracts. The e_2h_1 peak associated with domain III appears at voltages below -4.8 V, and its intensity increases with the current in the second transition region. The maximum intensity of the e_2h_1 PL from domain III occurs only at the onset of the next current plateau (-8 V). This again indicates that only domain III remains in the second transition region. The field strength of domain III approaches the condition of resonant tunneling only when it becomes a low-field domain (below -8 V). The voltage range of the second transition is much larger than that of the first transition. It implies that the width of the $e_1 \rightarrow e_3$ resonance is also much larger than that of the $e_1 \rightarrow e_2$ resonance. In the III-IV-V region, only the e_2h_1 signal from domain III can be observed. Its intensity decreases linearly as domain III contracts. Unfortunately, the e_2h_1 signals associated with domains IV and V are not observable due to the presence of a strong e_1h_1 PL background.

As expected, no e_3h_1 PL signal from domains I and II is detectable. The e_3h_1 PL associated with domain III only appears at voltages below -5 V indicating that the field strength of domain III is below the resonant field F_3 in the II-III region. Its behavior with voltage follows almost exactly that of the e_2h_1 PL. The strong correlation between the e_3h_1 and the e_2h_1 PL intensities demonstrates that the ratio of the electron population in e_3 to that in e_2 is rather constant in domain III. This is reasonable because most of the electrons in e_2 are produced by relaxation from e_3. Two e_3h_1 PL peaks are detected in the III-IV-V region as opposed to a triplet in the e_1h_1 PL spectra. Based on the separation of the e_1h_1 PL peaks associated with domains IV and V ($\sim$12 meV), the energy separation of e_3h_1 peaks associated with domains IV and V is calculated to be only $\sim$7 meV. After considering the peak width of e_3h_1 PL ($\sim$13 meV), we conclude that the two peaks associated with domains IV and V cannot be resolved. Moreover, no e_4h_1 signal is observable in the III-IV-V region, which indicates that domain IV is below the resonant field F_4.

The voltage dependence of the e_2h_1 and e_3h_1 PL intensities of sample 2 have been discussed in a previous publication.[19] Similar correlations between the e_jh_1 PL intensity and the photocurrent are seen. In the I-II re-

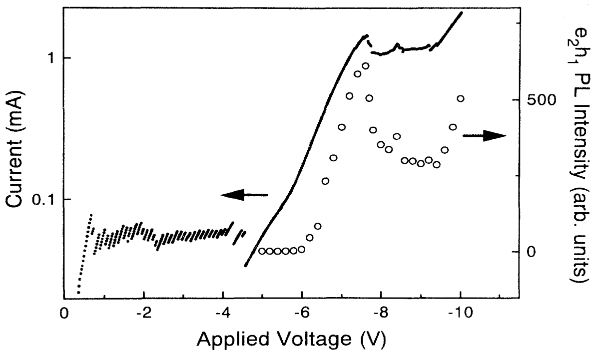

FIG. 6. Comparison between e_2h_1 PL intensity (open circles) and current (dots) vs applied voltage for sample 4.

gion (between 1.5 and −3.5 V), no e_2h_1 PL signal is seen. The e_2h_1 PL line indicating resonant alignment between e_1 and e_2 only emerges at voltages beyond −3.5 V and reaches its maximum intensity at −4.6 V. In the II-III region (between −4.6 V and −12.5 V), the absence of the e_3h_1 PL indicates again that the field strength of the high-field domain (III) is smaller than F_3. In the second transition region (between −12.5 V and −14 V), the e_3h_1 PL rises together with the current, implying that the field strength of domain III increases to a value equal to F_3 at ∼ −14 V. The intensities of the e_jh_1 PL and the photocurrent display maxima at the resonant voltages predicted by the measured subband spacings.

The number of periods, the barrier width, and the well width of samples 3 and 4 are the same. The only difference is that the doping in sample 4 leads to a two-dimensional electron density of about 1.5×10^{11} cm^{-2} in each well. In Fig. 6, we compare the e_2h_1 intensity with the current in sample 4. The photoexcited carrier concentration in this sample is negligible compared to the electron density due to doping. No significant e_2h_1 PL signal is seen in the first plateau region where domains I and II coexist. In the transition region, domain II occupies the entire superlattice. The intensity of the e_2h_1 PL and the current rise abruptly in this region. This again shows that domain II is under a resonant tunneling condition only when the onset of the next plateau is reached. For sample 3, the behavior of the e_2h_1 PL signal is similar. The e_2h_1 PL peak clearly emerges only during the first transition region. The maximum of the e_2h_1 PL intensity and the photocurrent occur at the same voltage (−4.6 V). For the undoped sample (sample 3), the above observations are also consistent with the resonant voltage predicted by the measured subband spacing. However, the onset voltage of the second plateau in the doped sample (sample 4) is considerably larger than the voltage estimated from the optical data. This is probably due to an additional voltage drop in the contact regions. The results of the e_2h_1 PL in the doped sample demonstrate that our observations are not related to photoexcitation.

V. CALCULATION OF THE FIELD DISTRIBUTION UNDER DOMAIN FORMATION

To explain our experimental observations, we use a transport model to calculate the *I-V* characteristics and field distribution in the superlattice.[17,28] We consider a superlattice with a period $d = l + b$, where l and b denote the widths of the GaAs well and the AlAs barrier, respectively.

For simplicity, we focus on the first and second subbands only, although an extension to higher subbands is straightforward. Denoting each well by a superscript (k), $k = 1, ..., N$, we have to find steady-state self-consistent solutions of the rate equations for the first subband

$$\begin{aligned}\dot{n}_1^{(k)} &= A^{(k)} + n_1^{(k-1)} R_1(F^{(k)}) - n_1^{(k)} R_1(F^{(k+1)}) \\ &\quad + n_2^{(k-1)} Y(-F^{(k)}) + n_2^{(k+1)} Y(F^{(k+1)}) \\ &\quad - n_1^{(k)} \left[X(-F^{(k)}) + X(F^{(k+1)}) \right], \end{aligned} \tag{4}$$

the second subband

$$\begin{aligned}\dot{n}_2^{(k)} &= -A^{(k)} + n_2^{(k-1)} R_2(F^{(k)}) - n_2^{(k)} R_2(F^{(k+1)}) \\ &\quad + n_1^{(k-1)} X(F^{(k)}) + n_1^{(k+1)} X(-F^{(k+1)}) \\ &\quad - n_2^{(k)} \left[Y(-F^{(k)}) + Y(F^{(k+1)}) \right], \end{aligned} \tag{5}$$

where the dot denotes the temporal derivative, and Poisson's equation

$$\epsilon\epsilon_0 (F^{(k+1)} - F^{(k)}) = el(n_1^{(k)} + n_2^{(k)} - N_D). \tag{6}$$

Here $F^{(k)}$ is the average field between the wells with index $(k-1)$ and (k) and N_D is the effective electron density provided by photoexcitation or doping in the wells. R_i is the rate of electrons crossing the barrier between two equivalent subbands with index i. We use the expression for the transport in a miniband $E_i(q) = E_i - \Delta_i \cos(qd)$

$$R_i = \frac{\Delta_i}{\hbar} \sqrt{\frac{\tau_m}{\tau_e}} \frac{F/\tilde{F}}{1 + (F/\tilde{F})^2} \tag{7}$$

with $\tilde{F} = \hbar/(ed\sqrt{\tau_m \tau_e})$. This expression has been derived in Ref. 29 where the influence of the different scattering times τ_m and τ_e for momentum and energy relaxation, respectively, has been considered. X and Y are the rate coefficients for resonant tunneling $e_1 \to e_2$ and $e_2 \to e_1$, respectively, calculated by perturbation theory.[17] The rates X and Y become small off resonance, but do not vanish due to the quantum mechanical energy uncertainty. Note that the inverse tunneling processes with $X(-F)$ and $Y(-F)$ are very small in general. In the low-field case they compensate the processes $X(F)$ and $Y(F)$.

The intersubband transition rate $A^{(k)}$ derived in Ref. 30 was used in Ref. 17 to solve the above equations. Meanwhile, we found that this expression is only valid for the resonant optical transitions and not for the optical-phonon scattering considered here. Thus, we use the simpler form $A^{(k)} = n_2^{(k)}/\tau_{21}$ with $\tau_{21} = 1$ ps now. (The two expressions differ only for high doping.)

We also note that the figures in Ref. 17 were obtained with a dielectric constant, which was two orders of magnitude too small. This resulted in the formation of domain states for very low doping. Stable domains similar to the result in Ref. 17 are found for a doping density N_D above 2×10^{17} cm^{-3}. All features, especially the multistability,[31] are qualitatively unchanged (see Ref. 28).

We model the contacts by the boundary conditions $n_i^{(0)} = n_i^{(1)}$ and $n_i^{(N+1)} = n_i^{(N)}$. The fields have to satisfy $U = d\sum_{k=1}^{N+1} F^{(k)}$ for fixed bias U. Figure 7(a) shows the resulting current density-field characteristic calculated for a model superlattice of $l = 9$ nm, $b = 1.5$ nm, and $N_D = 6.7 \times 10^{17}$ cm^{-3} with the restriction of a spatially homogeneous field distribution. The first maximum is due to miniband transport whereas the second, higher peak describes the $e_1 \rightarrow e_2$ tunneling resonance. In Fig. 7(b) the current-voltage characteristic is shown for the same superlattice with 40 wells for a sweep up of the voltage without the imposed restriction of homogeneity. The deviation from Fig. 7(a) indicates that an inhomogeneous field distribution has formed. The successive jumps correspond to a shift of the domain wall by one superlattice period, respectively, as illustrated by the corresponding field profiles in Fig. 8(a). The associated carrier densities are depicted in Fig. 8(b). One clearly sees that the sample decomposes into a low-field (I) and a high-field (II) domain, where the carrier density is equal to the doping density N_D, while negative charge accumulates around the domain boundary which extends only over a few periods. It follows that the sample breaks up into two coexisting regions where spatial homogeneity and charge neutrality hold, and which are, therefore, described by points on the local $J(F)$ characteristic of Fig. 7(a). Since due to current conservation the current through the low-field domain must equal the current through the high-field domain, the possible I-II domain states must lie on a horizontal line as indicated by the dashed line in Fig. 7(a). An upper and a lower bound for the possible currents of the I-II domain states are obviously given by the first maximum and the minimum of the $J(F)$ characteristic from Fig. 7(a). Note that these bounds are neither reached in the theoretical nor in the experimental characteristic (Fig. 6). The fields in domains I and II are always below the resonance fields F_1 and F_2, but the distance to resonance is much smaller in case of domain I than for domain II, which results from the shape of the homogeneous $J(F)$ characteristic.

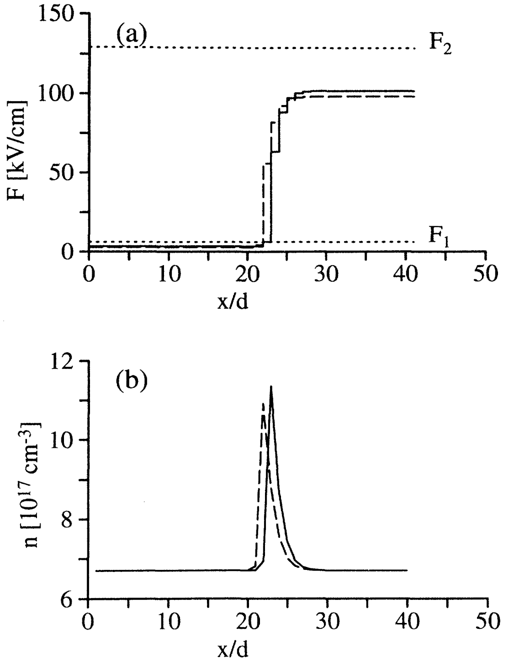

FIG. 8. Calculated field (a) and electron density (b) distribution before (full line) and after (dashed line) the jump marked by an arrow in Fig. 7(b).

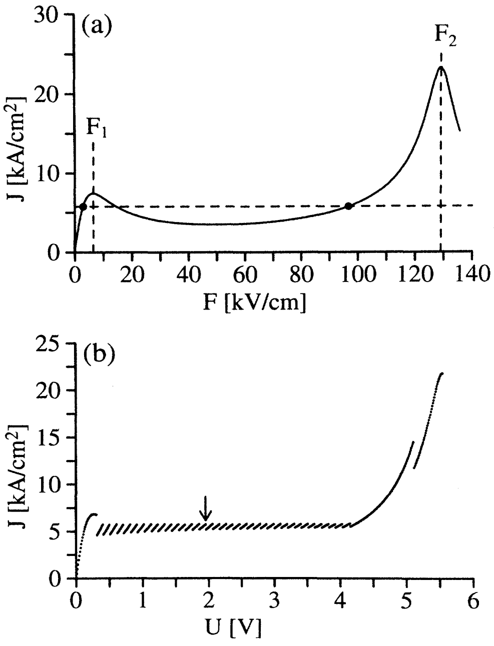

FIG. 7. (a) Calculated current-field characteristic. (Simulation parameters: $\epsilon = 13.18$, $\tau_{21} = 1$ ps, $\tau_e = 2$ ps, $\tau_m = 0.005$ ps, $E_1 = 44.6$ meV, $\Delta_1 = 1.4$ meV, $E_2 = 180.2$ meV, and $\Delta_2 = 6.1$ meV.) The two dots on the dashed line indicate possible coexisting domain states (see text). (b) Current-voltage characteristic for a sweep up of the voltage under domain formation.

With increasing voltage U both the fields in domain II and—albeit to a smaller extent—in domain I grow until the state becomes unstable and a new state forms, where the high-field domain grows by one superlattice period. This induces a vertical jump in the current-voltage characteristic, see Fig. 7(b). As the length of the high-field domain increases, the fields in both domains must decrease in order to keep the total voltage constant. Thus,

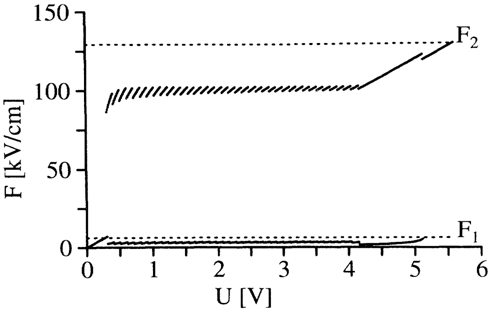

FIG. 9. Calculated electric field in the high-field (upper full lines) and low-field (lower full lines) domain depending on the external bias during the sweep up of Fig. 7(b). The dotted lines depict the resonant values F_1 and F_2.

the current is reduced after the jump. The slope of the domain branches of the current-voltage characteristic becomes successively smaller with increasing U since the effective resistance increases as the relative fraction of the high-field domain increases, in good agreement with the experiment (Fig. 6).

Finally, when the bias becomes large enough, the domain I vanishes and the current can increase beyond the left maximum in the $J(F)$ characteristic. (In our simulation this happens in a state which is still inhomogeneous. The chosen boundary condition seems to pin the inhomogeneity to the first barrier until a larger current is reached.) Then the field can reach the $e_1 \rightarrow e_2$ resonance value F_2. This explains the strong current increase in the first transition region and the strong emergence of the e_2h_1 PL intensity peak in Fig. 6 as the resonance is approached. While the general features of the model are in good agreement with the experiment we find a discrepancy in the occupation of e_2 in the I-II domain region. The model yields a small but nonvanishing occupation of e_2 due to the contribution of $X(F)$ at the nonresonant value of F in the high-field domain, while the PL data seem to exclude any occupation of the calculated order of magnitude. Of course the width of $X(F)$ is decreased if we use the experimental barrier width of 4 nm instead of 1.5 nm. Nevertheless, our nonresonant background is still too low. This indicates that the model overestimates the width of the resonance in X against nonresonant background currents between equivalent valleys. These might result from tunneling without in-plane momentum conservation.

Figure 9 summarizes the behavior of the fields in domain I (lower full lines) and domain II (upper full lines) with increasing voltage. It is clear that the fields are always below the respective resonance fields (dotted horizontal lines), and that the field in the uniform domain state (rightmost branch) increases monotonically to the resonance F_2. The model thus is in excellent agreement with the PL and photocurrent measurements. Analogous arguments hold for the II-III and higher domain states.

VI. SUMMARY AND CONCLUSIONS

In this paper we have performed a detailed study of the field distribution under electric field domain formation in superlattices. Table III compares the applied voltages for both the positions of maximal photocurrent and maximal e_jh_1 intensity with the voltage determined from the measured subband spacings. The good agreement of all values confirms that the current maxima are caused by resonant tunneling from e_1 into the corresponding higher subband leading to a large occupancy of the respective subband e_j. Thus, the intensity of the photoluminescence line e_jh_1 gives strong evidence for the resonant alignment of this level with e_1.

In the voltage range between the resonances $e_1 \rightarrow e_2$ and $e_1 \rightarrow e_3$ an oscillatory structure in the current-voltage characteristic appears. The fact that two e_1h_1 peaks arise clearly proves that two domains with different electric fields exist in this voltage region. Although the field in the high-field domain is close to the value of the $e_1 \rightarrow e_3$ resonance, the lack of a strong photoluminescence signal e_3h_1 indicates that the resonant field F_3 is not yet reached. Thus, the wells are coupled nonresonantly in this high-field domain. These features occur both for undoped samples under optical excitation and for doped samples.

The theoretical calculation yields a current-voltage characteristic and electric field profiles, which are qualitatively in good agreement with the experimental observation. We find that the interface region between the two field domains is of the order of two wells. The electric field is clearly below resonance condition in the high-field domain, but almost at the resonance field in the low-field

TABLE III. Applied voltages for resonant subband alignment.

Sample	$U_{1j}(e_1 \rightarrow e_j)$	From subband spacing (V)	From current maxima (V)	From e_jh_1 PL intensity maxima (V)
1	U_{12}	−1.8	−2.0	−2.0
	U_{13}	−7.4	−8.0	−7.4
2	U_{12}	−4.6	−4.8	−4.9
	U_{13}	−13.5	−14.0	−14.5
3	U_{12}	−4.7	−4.6	−4.7
4	U_{12}	−6.1	−7.4	−7.4

domain.

The question, which remains to be solved, concerns the nature of the nonresonant current in the high-field domain: do the carriers tunnel resonantly through virtual states of the second subband or is the transport governed by nonresonant tunneling from the bottom of the first subband into a higher energy state of the first subband in the adjacent well? In order to solve this question it is necessary to expand the existing theoretical approach to include the nonresonant channel.

ACKNOWLEDGMENTS

We would like to thank A. Fischer for sample growth, J. Kastrup for helpful discussions, Y. Takagaki for a critical reading of the manuscript, and R. Klann for experimental support. This work was supported in part by the Bundesminister für Forschung and Technologie and the DFG in the framework of Sfb 296 within the Federal Republic of Germany as well as by the U.S. Army Research Office under Contract No. DAAL-03-92-G-0233.

---

[1] R.F. Kazarinov and R.A. Suris, Fiz. Tekh. Poluprovodn. **5**, 797 (1971) [Sov. Phys. Semicond. **5**, 707 (1971)].
[2] F. Capasso, K. Mohammed, and A.Y. Cho, Appl. Phys. Lett. **48**, 478 (1986).
[3] H.T. Grahn, H. Schneider, and K. v. Klitzing, Phys. Rev. B **41**, 2890 (1990).
[4] L. Esaki and L.L. Chang, Phys. Rev. Lett. **33**, 495 (1974).
[5] Y. Kawamura, K. Wakita, H. Asaki, and K. Kurumada, Jpn. J. Appl. Phys. **25**, L928 (1986).
[6] K.K. Choi, B.F. Levine, R.J. Malik, J. Walker, and C.G. Bethea, Phys. Rev. B **35**, 4172 (1987).
[7] R.E. Cavicchi, D.V. Lang, D. Gershoni, A.M. Sergent, H. Temkin, and M.B. Panish, Phys. Rev. B **38**, 13 474 (1988).
[8] H.T. Grahn, H. Schneider, and K. v. Klitzing, Appl. Phys. Lett. **54**, 1757 (1989).
[9] E.S. Snow, S.W. Kirchoefer, and O.J. Glembocki, Appl. Phys. Lett. **54**, 2023 (1989).
[10] M. Helm, P. England, E. Colas, F. DeRosa, and S.J. Allen, Jr., Phys. Rev. Lett. **63**, 74 (1989).
[11] T.H.H. Vuong, D.C. Tsui, and W.T. Tsang, J. Appl. Phys. **66**, 3688 (1989).
[12] H.T. Grahn, R.J. Haug, W. Müller, and K. Ploog, Phys. Rev. Lett. **67**, 1618 (1991).
[13] I. Gravé, A. Shakouri, N. Kuze, and A. Yariv, Appl. Phys. Lett. **60**, 2362 (1992).
[14] D.A.B. Miller, D.S. Chemla, T.C. Damen, A.C. Gossard, W. Wiegmann, T.H. Wood, and C.A. Burrus, Phys. Rev. Lett. **53**, 2173 (1984).
[15] B. Laikhtman, Phys. Rev. B **44**, 11 260 (1991).
[16] A.N. Korotkov, D.V. Averin, and K.K. Likharev, Appl. Phys. Lett. **62**, 3282 (1993).
[17] F. Prengel, A. Wacker, and E. Schöll, Phys. Rev. B **50**, 1705 (1994).
[18] L.L. Bonilla, J. Galán, J.A. Cuesta, F.C. Martínez, and J.M. Molera, Phys. Rev. B **50**, 8644 (1994).
[19] S.H. Kwok, R. Merlin, H.T. Grahn, and K. Ploog, Phys. Rev. B **50**, 2007 (1994).
[20] A. Pinczuk and G. Abstreiter, in *Light Scattering in Solids V*, edited by M. Cardona and G. Güntherodt, Topics in Applied Physics Vol. 66 (Springer, Berlin, 1989), p. 153.
[21] K. Bajema, R. Merlin, F.-Y. Juang, S.-C. Hong, J. Singh, and P.K. Bhattacharya, Phys. Rev. B **36**, 1300 (1987).
[22] S. Murugkar, S.H. Kwok, G. Ambrazevičius, H.T. Grahn, K. Ploog, and R. Merlin, Phys. Rev. B **49**, 16 849 (1994).
[23] H.T. Grahn, H. Schneider, W.W. Rühle, K. v. Klitzing, and K. Ploog, Phys. Rev. Lett. **64**, 2426 (1990).
[24] H.T. Grahn, W.W. Rühle, K. v. Klitzing, and K. Ploog, Semicond. Sci. Technol. **7**, 3409 (1992).
[25] S.H. Kwok, H.T. Grahn, K. Ploog, and R. Merlin, Phys. Rev. Lett. **69**, 973 (1992).
[26] D. Bertram, H. Lage, H.T. Grahn, and K. Ploog, Appl. Phys. Lett. **64**, 1012 (1994).
[27] R. Ferreira and G. Bastard, Phys. Rev. B **40**, 1074 (1989).
[28] A. Wacker, F. Prengel, and E. Schöll, in *Proceedings of the 22nd International Conference on the Physics of Semiconductors*, edited by D. J. Lockwood (World Scientific, Singapore, in press).
[29] A. A. Ignatov, E. P. Dodin, and V. I. Shashkin, Mod. Phys. Lett. B **5**, 1087 (1991).
[30] R. E. Kunz and E. Schöll, Phys. Rev. B **47**, 4337 (1993).
[31] J. Kastrup, H. T. Grahn, K. Ploog, F. Prengel, A. Wacker, and E. Schöll, Appl. Phys. Lett. **65**, 1808 (1994).